# Electronic Supplementary Information (ESI)

# Direct dehydrogenation of methanol to formaldehyde over ZnO-SiO$_2$-based catalysts

Ankur Ghosh Chowdhury,[a] Ulrich Arnold,*[a] Krassimir Garbev,[b] Michael Bender[c] and Jörg Sauer[a]

[a]Institute of Catalysis Research and Technology (IKFT), Karlsruhe Institute of Technology (KIT), Hermann-von-Helmholtz-Platz 1, 76344 Eggenstein-Leopoldshafen, Germany

[b]Institute for Technical Chemistry (ITC), Karlsruhe Institute of Technology (KIT), Hermann-von-Helmholtz-Platz 1, 76344 Eggenstein-Leopoldshafen, Germany

[c]BASF SE, Carl-Bosch-Straße 38, 67056 Ludwigshafen am Rhein, Germany

*E-mail: ulrich.arnold@kit.edu

## Content

# Characterization of catalysts before catalytic tests

## BET surface areas and Zn contents

Table S1 contains a summary of the manufactured zinc silicate catalysts. The molar ratio of Zn:Si and the calcination temperature were the two primary variables during the synthesis process. These variables can be individually correlated to the measured catalyst properties namely BET area and Zn content.

**Table S1** BET surface areas and Zn contents of the zinc silicates

| Catalyst | Zn:Si molar ratio | Calcination temperature under air [°C] | BET surface area [$m^2\ g^{-1}$] | Zn content [wt%] |
|---|---|---|---|---|
| ZS1-C1 | 0.75 | 600 | 161.1 | 32 |
| ZS1-C2 | 0.75 | 900 | 24.9 | 36 |
| ZS2-C1 | 1.0 | 600 | 123 | 38 |
| ZS2-C2 | 1.0 | 900 | 19.9 | 38 |
| ZS3-C1 | 1.5 | 600 | 73.9 | 47.7 |
| ZS3-C2 | 1.5 | 900 | 26 | 59.8 |
| ZS4-C1 | 2.0 | 600 | 73.1 | 48.4 |
| ZS4-C2 | 2.0 | 900 | 32.3 | 61.9 |

## XRD analysis

Fig. S1(a) shows how the crystallinity within the materials develops with an increase in the zinc content at a calcination temperature of 900 °C. The highest peak positioned at 2θ of 37° corresponds to the ZnO crystal structure, which is the initial crystalline phase that develops within all materials. As the Zn content is increased, crystalline phases are also indicated at 34° and 31.52°. These peaks correspond to zinc silicate structures represented by $Zn_2SiO_4$. From Fig. S1(b) it can be seen that the signals at 22-23° and 25-27° belong to the zinc silicates, viz. α-$Zn_2SiO_4$ and β-$Zn_2SiO_4$, respectively. These crystalline phases are absent for all C1 materials, which were calcined at 600 °C. It was concluded that, in order to obtain high crystalline zinc silicates, the temperatures have to be precisely higher than 875 °C as well as the Zn:Si ratio should be at least above 1 [1]. ZnO to $SiO_2$ diffusion can only take place above this temperature and furthermore, the lesser amount of Zn present in the material only leads to ZnO formation, rather than stable zinc silicates. However, as the ratio of Zn:Si increases considerably, this leads to the formation of free ZnO, probably because of the non-availability of unbound $SiO_2$ in order for it to react spontaneously. This phenomenon has a rather adverse implication for its usage as a catalyst.

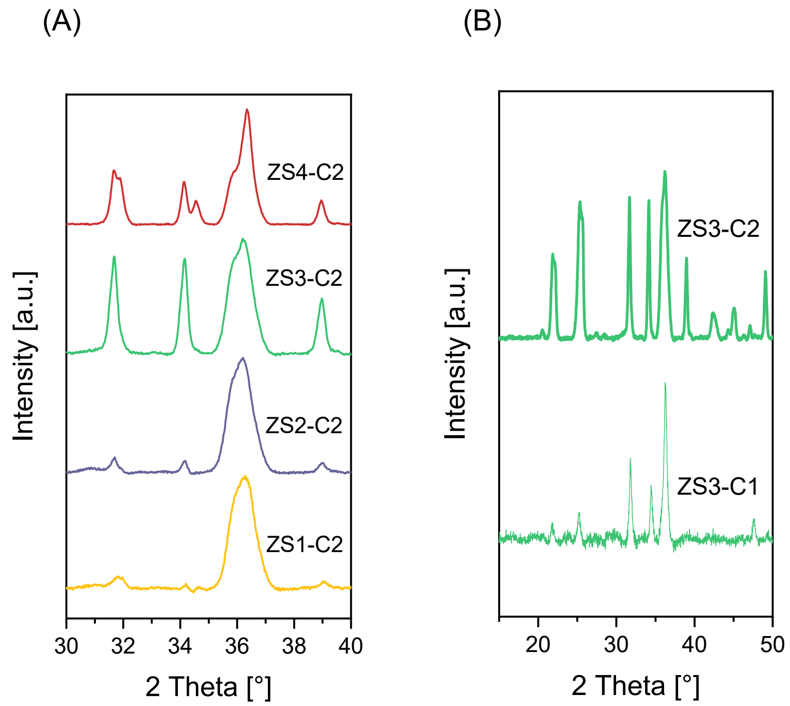

**Fig. S1** XRD patterns of the zinc silicates as a function of (A) Zn:Si ratio and (B) calcination temperature.

### Quantification of phases within zinc silicates

Direct Rietveld refinement of the samples was not possible due to the lack of structural data for β-$Zn_2SiO_4$. Even the space group is not known, but is assumed to be an orthorhombic one. Therefore, the reflections of β-$Zn_2SiO_4$ were fitted by introducing peaks on the positions of the observed reflections corresponding to those in ICDD card 14-0653. For α-$Zn_2SiO_4$ and ZnO the structures from the ICSD entries 257027 and 34474 were used, respectively. Additional problem poses the presence of a broad hump at 30.82° 2θ, which does not belong to β-$Zn_2SiO_4$ and is possibly due to an excess of $SiO_2$. Thus, an additional peak was introduced to the refinement separately calculated from the peaks of β-$Zn_2SiO_4$.

The refinement was performed with the fundamental parameters approach implemented in TOPAS v.6 (Bruker AXS, Karlsruhe, Germany). The degree of crystallinity (DOC) method, based on the estimation of the total area contribution by each component in the diffraction pattern, was used to calculate the weight fraction of both components defined as “amorphous”, β-$Zn_2SiO_4$ and the unknown phase giving rise to the peak at 30.82°. The calculation was performed by the following formulae:

1) $DOC_1$ = [Crystalline area (fraction α-$Zn_2SiO_4$ + fraction ZnO)] / [Crystalline area + (amorphous area β-$Zn_2SiO_4$)]
2) $DOC_2$ = [Crystalline area (fraction α-$Zn_2SiO_4$ + fraction ZnO )] / [Crystalline area + (amorphous area β-$Zn_2SiO_4$ + amorphous area at 30.82° 2θ)]

The weight fractions $W_{\beta\text{-}Zn2SiO4}$ = 1-$DOC_1$ and $W_{30.82°}$ = $DOC_1$-$DOC_2$ were calculated separately by two iterations. Given the both polymorphic modifications, have same chemical compositions and thus equal mass absorption coefficients (MAC), their weight proportions were directly calculated from the areas. The quantitative results for the crystalline phases (α-$Zn_2SiO_4$ and ZnO), which always sum to 100 wt%, were proportionally distributed within $DOC_2$. The results are listed in Table S2 as wt% of the three phases (ZnO, α-$Zn_2SiO_4$ and β-$Zn_2SiO_4$) alongside wt% of the amorphous structures inside the zinc silicates.

**Table S2** Parameters for the quantification of phases within the zinc silicates

| Catalyst | Rietveld | | $DOC_1$ | $DOC_2$ | 1-$DOC_1$ | $DOC_1$-$DOC_2$ |
|---|---|---|---|---|---|---|
| | α-$Zn_2SiO_4$ [wt%] | ZnO [wt%] | β-$Zn_2SiO_4$ | β-$Zn_2SiO_4$ + unknown | β-$Zn_2SiO_4$ [wt%] | Amorphous [wt%] |
| ZS1-C2 | 60.0<br>6.0 | 40.0<br>4.0 | 20.0 | 10 | 80.0<br>80.0 | 10<br>10 |
| ZS2-C2 | 65.0<br>6.3 | 35.0<br>3.0 | 18.9 | 9.3 | 81.1<br>81.1 | 9.6<br>9.6 |
| ZS3-C2 | 95.8<br>48.6 | 4.2<br>2.1 | 56.8 | 50.7 | 43.2<br>43.2 | 6.1<br>6.1 |
| ZS4-C2 | 48.7<br>19.2 | 51.3<br>20.2 | 46.2 | 39.4 | 53.8<br>53.8 | 6.8<br>6.8 |

## Raman spectroscopy

Fig. S2 shows a 20x20 µm Raman mapping of the phase distribution in the fresh sample of ZS3-C2 as a Raman image in false colors. The optical image of an aggregate of α-$Zn_2SiO_4$ on β-$Zn_2SiO_4$ surface is shown in Fig. S2(A). The Raman image is overlaid on the optical picture in (B). The basic spectra of α-$Zn_2SiO_4$, β-$Zn_2SiO_4$ and ZnO used for the creation of the Raman image are shown in (C). Four peaks at about 200 $cm^{-1}$ (very weak), 330 $cm^{-1}$, 435 $cm^{-1}$ (very strong) and a broad peak at 520 $cm^{-1}$ with shoulder at 545 $cm^{-1}$ dominated the Raman spectra of ZnO (zincite). The band at 437 $cm^{-1}$ is assigned to E 2 (high) mode. The bands at 200 and 330 $cm^{-1}$ are assigned as 2E 2 (low) and E2 (high) – E 2 (low) modes, respectively. The broad band at 520 $cm^{-1}$ is assigned to an IR active E1(L), which is observable in Raman due to defective structure [2–5].

α-$Zn_2SiO_4$ (willemite) crystallizes in the rhombohedral space group (No.148) and shows a strong band at 870 $cm^{-1}$ assigned to the symmetrical stretching $\nu_1$-[Si-$O_4$] [6]. Additional bands assigned to $\nu_3$-[Si-$O_4$] modes are visible at 905 and 944 $cm^{-1}$. The corresponding bending modes $n_2$ and $\nu_4$-[Si-$O_4$] occur at 378 as well as 397 $cm^{-1}$ and at very low intensity in the 460-

490 cm$^{-1}$ range, respectively. Modes of the stretching [Zn-O$_4$] vibrations can be seen at 548 cm$^{-1}$ and in the range of 590-620 cm$^{-1}$ [7].

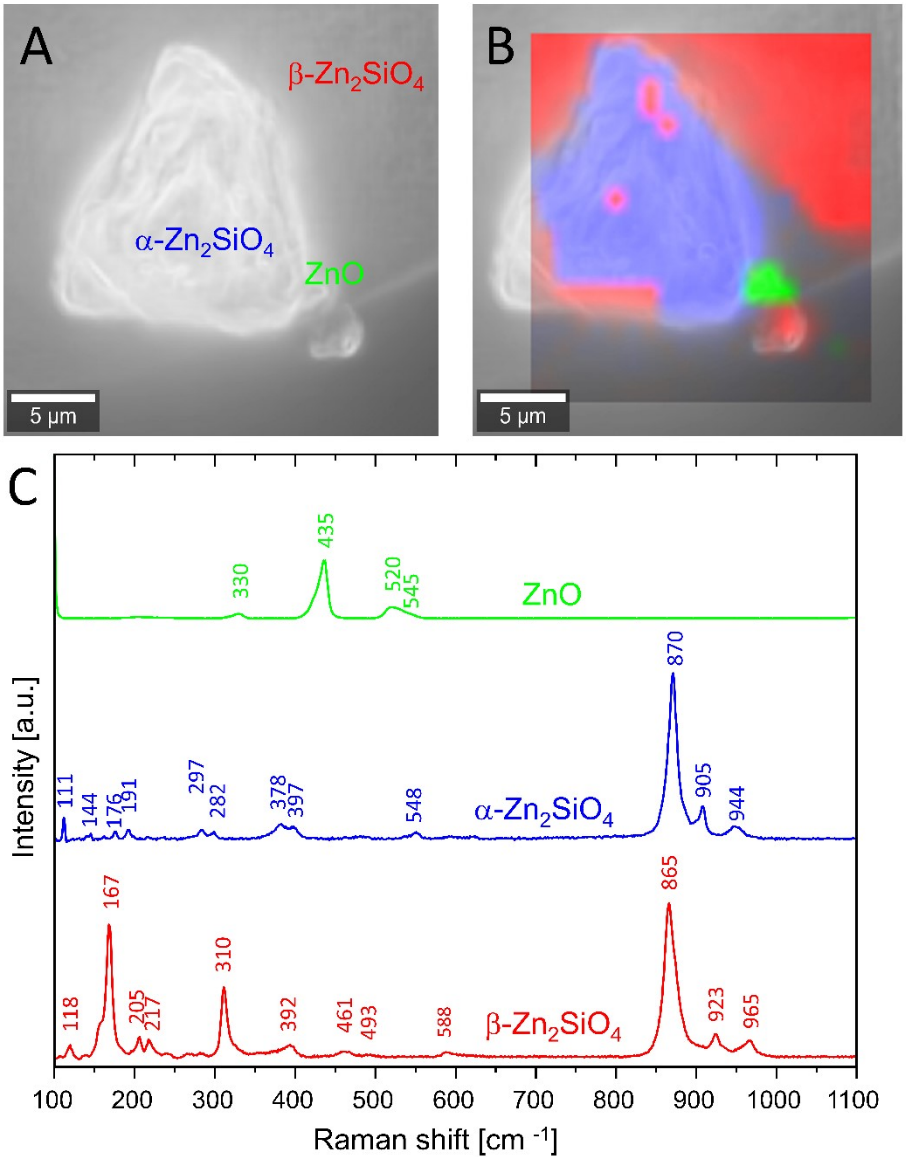

**Fig. S2** Optical and Raman images of CS3-C2 before reaction: A Optical image of an aggregate of α-Zn$_2$SiO$_4$ on β-Zn$_2$SiO$_4$ surface; B Raman image overlay on the optical picture; C Basic spectra of α-Zn$_2$SiO$_4$, β-Zn$_2$SiO$_4$ and ZnO used to produce the phase distribution of the Raman image in B.

There are just a few studies reporting Raman spectra of the orthorhombic β-Zn$_2$SiO$_4$, mostly in mixtures with other compounds [8–10]. In this study we show for the first time a pure Raman spectrum of this phase, verified by multiple high-resolution measurements and to highlight its differences from α-Zn$_2$SiO$_4$. One striking difference is the positions of the stretching Si-O$_4$ bands. In the spectrum of β-Zn$_2$SiO$_4$, the symmetrical $\nu_1$-[Si-O$_4$] mode occurs as the most intense band at 865 $cm^{-1}$, whereas the analogous band in α-$Zn_2SiO_4$ is positioned at 870 $cm^{-1}$. The corresponding $\nu_3$-[Si-$O_4$] mode gives rise to bands at 923 $cm^{-1}$ and 965 $cm^{-1}$ (with a shoulder at 955 $cm^{-1}$) in the spectra of β-$Zn_2SiO_4$ and at 905 and 944 $cm^{-1}$ in the case of α-$Zn_2SiO_4$. The positions of the stretching modes in the Raman spectra of α-$Zn_2SiO_4$ show strong dependence from the FWHM of the bands. In addition, the spectra of β-$Zn_2SiO_4$ show strong bands at 167 $cm^{-1}$ and 310 $cm^{-1}$ [10]. Interestingly, similar bands are observed in the orthorhombic structure of the high pressure phase II of $Zn_2SiO_4$ described in the I-42d space group [11,12]. Very specific is the sharp doublet with low intensity at 205 $cm^{-1}$ and 217 $cm^{-1}$. Further bands include 117 $cm^{-1}$, 238 $cm^{-1}$ (probably due to Zn-O bending vibrations), 392 $cm^{-1}$, 461 $cm^{-1}$ and 493 $cm^{-1}$ ($\nu_2$ and $\nu_4$ Si-$O_4$) and 588 $cm^{-1}$ ($\nu_1$-Zn-$O_4$).

## Characterization of catalysts after catalytic tests

### XRD analysis

The instability of the ZnO and β-$Zn_2SiO_4$ phases was investigated with the help of quantitative XRD analysis. Fig. S3 shows ZS3-C2 and ZS4-C2 materials, which were contested during MST experiment. It was revealed that the amount of ZnO present in both the materials showed a decreasing trend after the catalytic tests. In addition, the β-$Zn_2SiO_4$ phase within the material decreased considerably for the ZS4-C2 material and for the ZS3-C2 material. The loss in the β-$Zn_2SiO_4$ phase was compensated by an increase in the wt% of α-$Zn_2SiO_4$. The crystallinity of the material increased. The quantification of the active phases of the material, led to the conclusion that the α-$Zn_2SiO_4$ was the most stable phase out of the three. This phase was probably also responsible for the methanol activity. Since, from the ZS1-C2 and ZS2-C2 materials, it was known that the β-$Zn_2SiO_4$ illustrated very low to no activity.

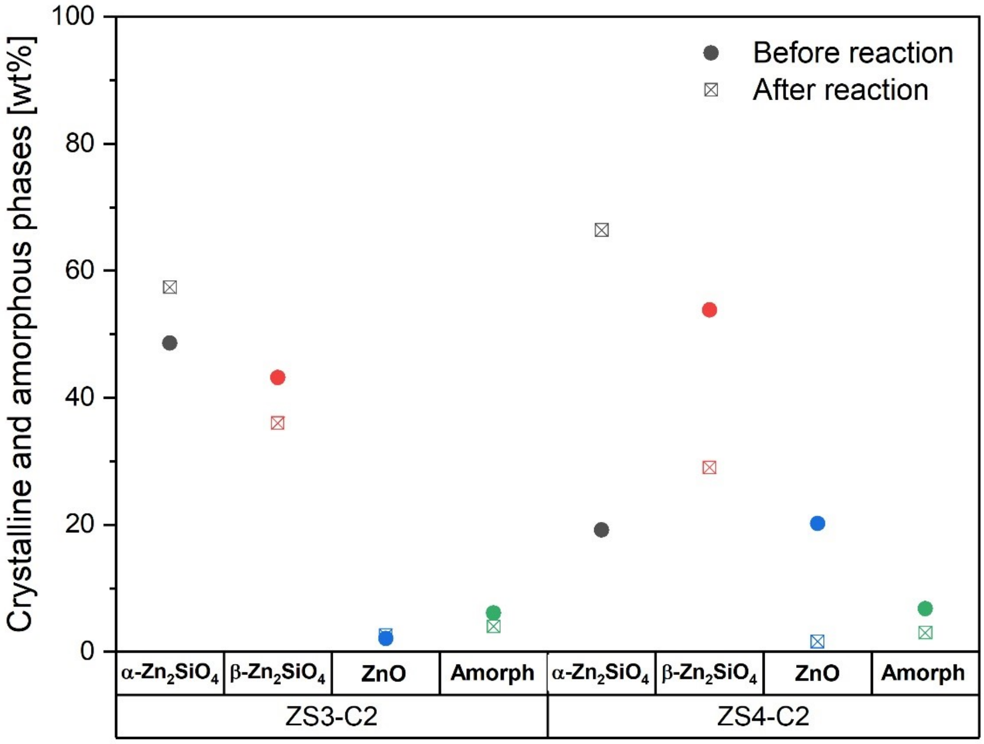

**Fig. S3** Content of crystalline and amorphous phases in the ZS3-C2 and ZS4-C2 materials before and after reaction.

## Raman spectroscopy

Fig. S4 reveals an optical image of the ZS3-C2 catalyst tested in the context of a time on stream (TOS) experiment. By comparing the fresh material to the spent catalyst there are two clear observations, which can be made. The absence of β-$Zn_2SiO_4$ phase alongside coke deposition are the two phenomena, which can be observed. The absence of the β-$Zn_2SiO_4$ phase was also observable from the XRD analysis. It is important to say that the coke deposition is a type of unorderly fashioned, almost like a graphene like structure. Presence of ZnO can be from the previously present loose ZnO from fresh material. It is important to mention here, that similar Raman imaging were performed repetitively, in order to review and concrete the absence of β-$Zn_2SiO_4$ phase within the catalyst.

**Fig. S4** Optical and Raman images of CS3-C2 after reaction: A Optical image of ZS3-C2 catalyst from TOS experiment with overlaid Raman mapping; B Basic spectra of $\alpha$-$Zn_2SiO_4$, ZnO and carbon; C Zoomed in Raman imaging of the ZS3-C2 material, where all the phases have been depicted individually and once combined.

## Zinc loss of the C2 catalysts during the catalytic tests

The catalytic tests resulted in different amounts of Zn loss within the tested C2 materials. In general, materials with higher contents of zinc silicate phases inside the matrix exhibited lower Zn loss. The respective results are summarized in Table S3.

**Table S3** Zn loss of the C2 catalysts after reaction

| Catalyst | Zn loss (spent catalyst after 3.5 h) [wt%] |
|---|---|
| ZS1-C2 | 0.1 |
| ZS2-C2 | 1.2 |
| ZS3-C2 | 2.9 |
| ZS4-C2 | 16 |

## Coking and Zn loss of ZS3-C2 catalyst

In order to understand the reasons for catalyst deactivation, various TOS experiments were carried out employing the ZS3-C2 catalyst (Fig. S5). Here, the catalyst reached a stable conversion after almost 16 h TOS. Within the first 8 hours of operation, a significant Zn loss could be observed. Simultaneously, this phenomena is combined with catalyst coking. As the reaction proceeds the overall deactivation reduces and the conversion becomes relatively stable after 16 h TOS. After this, specifically, the amount of Zn loss decreases much more than the amount of catalyst coking. Therefore, it can be suggested that initially free ZnO, which is not chemically combined with silica is reduced leading to higher Zn loss. After the first 8 h, as the reaction proceeds and the free ZnO is reduced, coking becomes the primary reason of catalyst deactivation. A possibility of zinc silicate decomposition, thereby leading to further zinc loss cannot be completely ruled out.

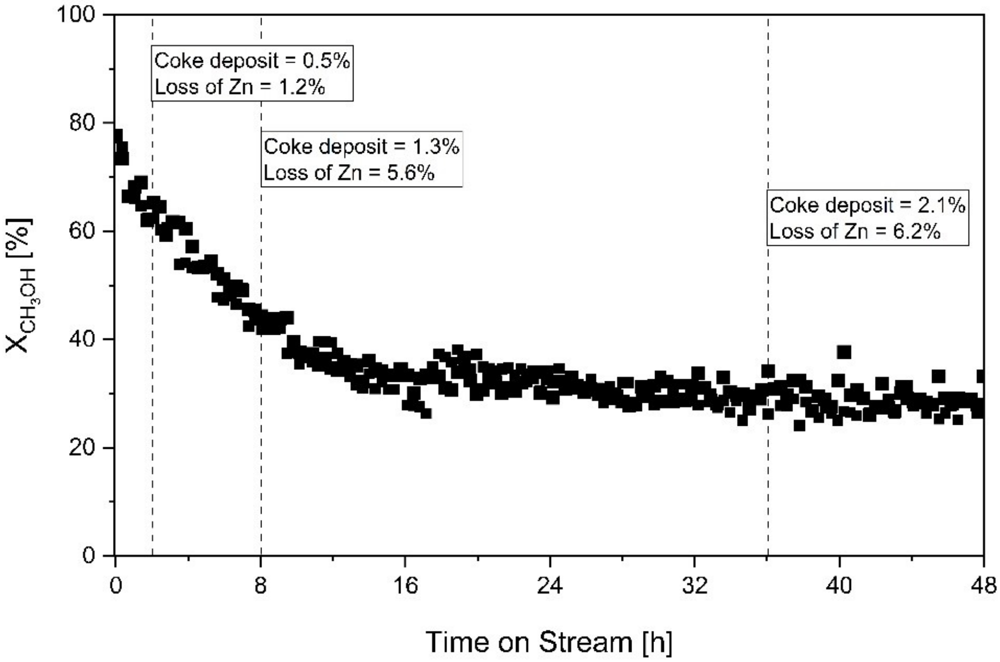

**Fig. S5** Time on stream experiment to determine catalyst coking and deactivation (Reaction conditions: 2.6% $CH_3OH$ in $N_2$ as carrier gas, 200 mg of catalyst and T = 550 °C).

## References

1 M. Takesue, H. Hayashi and R. L. Smith, Thermal and chemical methods for producing zinc silicate (willemite): A review, *Progress in Crystal Growth and Characterization of Materials*, 2009, **55**, 98–124.

2 J. M. Calleja and M. Cardona, Resonant Raman scattering in ZnO, *Phys. Rev. B*, 1977, **16**, 3753–3761.

3 J. Serrano, A. H. Romero, F. J. Manjón, R. Lauck, M. Cardona and A. Rubio, Pressure dependence of the lattice dynamics of ZnO: An ab initio approach, *Phys. Rev. B*, 2004, **69**.

4 F. J. Manjón, B. Marí, J. Serrano and A. H. Romero, Silent Raman modes in zinc oxide and related nitrides, *Journal of Applied Physics*, 2005, **97**, 53516.

5 S. Guo, Z. Du and S. Dai, Analysis of Raman modes in Mn-doped ZnO nanocrystals, *phys. stat. sol. (b)*, 2009, **246**, 2329–2332.

6 B. Chandra Babu and S. Buddhudu, Analysis of structural and electrical properties of Ni2+:Zn2SiO4 ceramic powders by sol–gel method, *J Sol-Gel Sci Technol*, 2014, **70**, 405–415.

7 I. M. Alibe, K. A. Matori, H. A. A. Sidek, Y. Yaakob, U. Rashid, A. M. Alibe, M. H. M. Zaid, S. Nasir and M. M. Nasir, Effects of polyvinylpyrrolidone on structural and optical properties of willemite semiconductor nanoparticles by polymer thermal treatment method, *J Therm Anal Calorim*, 2019, **136**, 2249–2268.

8 P. Loiko, O. S. Dymshits, V. V. Vitkin, N. A. Skoptsov, A. A. Zhilin, D. V. Shemchuk, M. Y. Tsenter, K. Bogdanov, A. M. Malyarevich, I. V. Glazunov, X. Mateos and K. V. Yumashev, Saturable absorber: transparent glass-ceramics based on a mixture of Co:β-Zn2SiO4 and Co:ZnO nanocrystals, *Applied optics*, 2016, **55**, 5505–5512.

9 C. Lin, J. Wang, X. Zhao, E. Zhu, N. Long and C. Rüssel, Competitive crystallization of β-Zn2SiO4 and ZnO in an aluminosilicate glass, *Ceramics International*, 2018, **44**, 7209–7213.

10 M. Sharma, G. Singh and R. Vaish, Transparent glass-nanocomposites possessing piezoelectric ZnO/Zn 2 SiO 4 nanocrystallites for piezocatalytic dye degradation, *Environ. Sci.: Water Res. Technol.*, 2023.

11 M. Kanzaki, Pressure–induced phase transitions of $Zn_2SiO_4$ III and IV studied using in–situ Raman spectroscopy, *Journal of Mineralogical and Petrological Sciences*, 2018, **113**, 263–267.

12 F. Marumo and Y. Syono, The crystal structure of Zn2SiO4-II, a high-pressure phase of willemite, *Acta Crystallogr B Struct Crystallogr Cryst Chem*, 1971, **27**, 1868–1870.